Prediction of cavitation and induced erosion inside a high-pressure fuel pump

P. Koukouvinis[1], I.K. Karathanassis[1,*], M. Gavaises[1]

[1]*School of Mathematics, Computer Science and Engineering, City, University of London, Northampton Square, EC1V 0HB London, UK*

Foivos.Koukouvinis.1@city.ac.uk, Ioannis.Karathanassis@city.ac.uk, m.gavaises@city.ac.uk

[*]Corresponding author

Abstract. The operation of a high-pressure, piston-plunger fuel pump, oriented for use in the common rail circuit of modern Diesel engines for providing fuel to the injectors is investigated in the present study from a numerical perspective. Both the suction and pressurization phases of the pump stroke were simulated with the overall flow time being in the order of $12 \cdot 10^{-3}$ s. The topology of the cavitating flow within the pump configuration was captured through the use of an Equation of State (EoS) implemented in the framework of a barotropic, homogeneous equilibrium model. Cavitation was found

to set in within the pressure chamber as early as $0.2 \cdot 10^{-3}$ s in the operating cycle, while the minimum liquid volume fraction detected was in the order of 60% during the second period of the valve opening. Increase of the in-cylinder pressure during the final stages of the pumping stroke lead to the collapse of the previously arisen cavitation structures and three layout locations, namely the piston edge, the valve/valve-seat region and the outlet orifice, were identified as vulnerable to cavitation-induced erosion through the use of cavitation-aggressiveness indicators.

Short title: Cavitation in high-pressure pump.

Keywords: Diesel, common rail system, high pressure, barotropic model, moving valve

Nomenclature

a	volume fraction (-)
B	bulk modulus
C	constant of ideal gas Eq. (1b)
c	speed of sound (m/s)
C_p	specific heat (J/kgK)
h_{fg}	latent heat of vaporization (J/kg)

Ja	Jakob number (-)
n	constant of Tait Eq. (1a)
p	pressure (Pa)
T	temperature (K)
t	time (s)
u	velocity (m/s)

Greek symbols

γ	heat-capacity ratio (-)
μ	dynamic viscosity (Pa·s)
ρ	density (kg/m3)

Subscripts/Abbreviations

c	chamber
HEM	homogeneous equilibrium model
l	liquid
ref	reference
sat	saturation
v	volume

1. Introduction

Emission legislations for vehicles equipped with IC engines, e.g. Euro 6 and Tier IV standards in EU and USA, respectively, force modern manufactures to develop environmentally friendly engines able to cope with a variety of high-quality fuels and biofuels. The electronically controlled high-pressure common rail system has a vital impact on the engine performance, reliability and pollutant formation levels. Hence, significant attention has been given in the recent years to the design evaluation of the various common-rail system sub-components and novel layouts have been proposed referring to the fuel-injectors configuration and the high-pressure pump feeding them[1].

Cavitation is a characteristic flow phenomenon encountered in a wide range of engineering applications such as marine propellers and rudders, bearings, turbines[2], fuel injectors[3], and pumps[4]. The highly transient and uncontrollable nature of the phenomenon can have a detrimental impact on a device leading to the deterioration of its performance and the wear of its rigidity due to the emergence and subsequent violent collapse of vapour bubbles, along with other undesirable consequences such as noise and vibrations. Referring hydrodynamic machinery, the performance deterioration and reliability issues of hydraulic turbines, pumps or pump–turbines associated with the formation of cavitation-flow phenomena occurring in either the moving/rotating or stationary parts of the machines have been summarized by Avellan[5]. Schmidt et al.[6] correlated the emergence of cloud-cavitation structures identified through high-speed visualization with acoustic measurements in reference to a pump-turbine.

Especially in the case of positive-displacement pumps cavitation is possible to occur due to throttling effects induced by the geometrical layout and the conditions of operation. Geometrical modifications in order to mitigate the effect of cavitation within axial-piston pumps have been proposed by Wang[7] and Kumar and Bergada[8]. Furthermore, the use of pumps of such type for liquid delivery induces pulsating flow inside the hydraulic circuit, accompanied by the formation of pressure waves that propagate through the fluid and the solid components and could be responsible for mechanical fatigue and failure of hydrodynamic components. The numerical study of Ni et al.[9] elucidated the effect of air content on the peak pressures within the hydraulic circuit including a vane rotating oil pump. Higher air content was found to increase the intensity of the pressure pulse within the hydraulic circuit. Frosina[10] numerically investigated the operational characteristics of a variable-displacement oil pump comprising a rotor and a static shell. Their three-dimensional model was validated against experimental data in terms of mass flow rate as a function of the pump rotational speed. Cavitation effects were considered and the flow-path regions where vapour pockets emerge were identified.

There are limited studies available in the literature that discuss the development of two-phase flow in positive-displacement pumps bearing a piston-plunger and a separate pressurization chamber, where cavitation can also emerge during the phases of volume expansion. Petzold et al.[11] visualized the transient, two-phase flow within a metering pump employing a closed chamber pressurized by a moving piston. Two variations of the configuration were considered, bearing different port-hole designs, in order to verify which one achieved higher dosage accuracy designated by the extent of bubble growth in the pump chamber. Giuffrida et al.[12] investigated, in terms of liquid delivery efficiency, the operation of a radial positive displacement pump comprising three separate pressurization chambers and three plungers connected through a common cam ring. It was verified that the delivered flow rate decreased for increasing values of the pump driving speed and constant

delivery pressure. This trend was attributed to the onset of cavitation during the pump suction period at high cam rotational speed.

From a numerical modelling point of view, the studies available so far that refer to positive-displacement pumps adopt a series of simplifications regarding either the prevailing flow conditions or the moving components of the geometrical layout. Iannetti et al.[13] evaluated the effect of the non-condensable air-mass fraction on the cavitation phenomena occurring within a positive-displacement water pump using a two-phase mixture model. The two-phase field arising within an axial piston oil-pump, where the flow enters the compression chamber through a V-shaped slit was investigated by Tsukiji et al.[14] using both flow visualization and a numerical model. The comparison of flow visualization data with CFD predictions revealed that the extent of the vapour cloud emerging at the location of geometrical constriction can be accurately captured by the numerical model. However, only the case of a static piston close to its upper dead state was considered. Roemer et al.[15] performed a dynamic-mesh simulation, in order to predict the compressible flow emerging within a chamber connected to high and low-pressure manifolds, a layout that corresponds to a simplified unit-cell of a digital-displacement pump. Husmeier et al.[16] used an Eulerian-Eulerian multiphase model along with a moving-mesh technique, in order to predict the two-phase field that emerges inside a fuel-delivery pump, where the inlet manifold and discharge nozzle are obliquely located on top of a pressurization chamber.

Apart from the reduction in pump delivery efficiency associated with the onset of cavitation, the collapse of cavitation bubbles poses a threat to the structural integrity of the device itself, as well as to other components of the common rail system, as it can lead to the introduction into the main flow of metallic particles separated from the material surfaces. Cavitation-induced erosion may be attributed to two primary mechanisms, namely either to the impingement of pressure waves emitted during the bubble implosion on material surfaces or to the impulse momentum of a liquid micro jet

created due to the asymmetrical bubble collapse that impinges on the solid surface[17]. Dular et al.[18] developed an erosion model based on the concept of liquid microjet impingement. It was established through numerical simulations and measurements on a hydrofoil indicated that material damage is closely connected to cavity unsteadiness with cavitating vortical structures identified as more aggressive in terms of erosion inducement. Fortes-Patella et al.[19] correlated the material damage caused by cavitation erosion to the characteristics of pressure waves emitted by the collapse of vapour structures. It was predicted and experimentally verified that the wave power density was in close connection to the pit volume created on the material surface. Li[20] numerically predicted cavitating flows in various geometrical layouts and concluded that the maximum pressure temporal derivative is a well-suited criterion for predicting cavitation erosion, while, on the contrary, high change-rate of the vapour volume fraction did not correlate well with erosion damage. Koukouvinis et al.[21] have proposed a series of indicators, such as the pressure and volume fraction total (material) derivatives, suitable for the identification of flow regions were cavitation-induced erosion is most likely to set in. Comparison of the predicted regions of high cavitation aggressiveness against erosion data available for an axisymmetric throttle device demonstrated the validity of the employed indices.

Studies focusing on the factors affecting the development of cavitation erosion especially in reference to pumping devices are scarce in the literature and mainly focus on radial-flow configurations. Timushev et al.[22] evaluated two centrifugal-pump designs in terms of sensitivity to cavitation-induced erosion. It was deduced by the authors that the probability of surface-erosion occurrence, was dependent on the pressure gradient normal to the impeller wall. Sedlář et al.[23] analysed the cavitating flow within a two-stage radial pump by also considering bubble-dynamics aspects, such as a non-uniform distribution of the bubbles initial size and the collapse and rebound sequence of va-

pour bubbles. The pump impeller region with the highest erosion risk was specified as the location where the first collapse of bubbles occurs at flow trajectories close to the solid surface

The focus of the present study is to illustrate the cavitation phenomena that occur inside a high-pressure, positive-displacement, fuel pump suitable for feeding the injectors of a Diesel-engine common rail system. The main objective is to pinpoint the regions of the device layout where extensive generation and subsequent collapse of vapour bubbles takes place. In order to accomplish that, a robust Homogeneous Equilibrium Model has been developed and employed in the simulations. The determination of the overall vapour-occupied volume within the pressure chamber during the operation cycle allows an estimation to be made on the pump delivery efficiency, while, furthermore the near-wall sites of bubble collapse exhibit high risk of erosion. Various indices have been employed to quantify the aggressiveness of cavitation collapse.

2. Geometrical configuration and operating conditions

The high-pressure, diesel fuel pump considered in the present investigation is depicted in **Fig. 1**. The pump in question is of the positive-displacement type, comprising a manifold section and a sealed chamber connected through a moving valve. The liquid is pressurized within the chamber through the translational movement of a piston plunger. The pump receives diesel fuel from a low-pressure pump, not examined here, at a pressure of $6.5 \cdot 10^5$ Pa and temperature approximately equal to 318 K. The duration of the pumping cycle for the purposes of the present investigation was taken equal to $12 \cdot 10^{-3}$ s with the main interest being to elucidate the development of the cavitation topology during the suction period of the pump operation and mainly at part load conditions, where throttling is applied in the pump inlet, to limit the maximum delivered fuel.

The main geometrical components comprising the pump layout are also indicated in **Fig. 1**. Note that the pump geometry is symmetrical in respect to the XZ plane. The pump inlet that directs fuel

into the manifold volume can be discerned at the upper left part of **Fig. 1a**. It must be noted that the cross-section of the inlet pipe has been adjusted according to the throttling applied, in order to simulate the part-load condition effect. The manifold volume has a ring shape with semi-circular cross section and acts as a buffer volume, to absorb sharp transient effects. Four circular pipes, placed in a cross pattern, connect the manifold volume with the pump cylinder entrance. A mushroom-shaped valve, as illustrated in the section-view of **Fig. 1b**, is located at the cylinder entrance, to prevent liquid from counter-flowing towards the inlet during the compression phase. In the instance shown in **Fig. 1** the valve lift is 1.0 mm, while the maximum valve lift is approximately equal to 1.6 mm. A moving piston wall located at the bottom of the cylinder volume, which can also be seen at the lower part of **Fig. 1b**, represents the pump plunger. The piston is depicted at its top dead-centre point corresponding to the minimum cylinder volume. The piston displacement during the pump stroke follows a sinusoidal motion with 5mm amplitude. Finally, the pressurized liquid exits the pump through a cylindrical duct. In the actual device, a check valve is employed at the duct outlet that opens when the desired pressure is reached, i.e. approximately $2000 \cdot 10^5$ Pa. In this work the outlet valve is omitted and replaced with a wall; thus, the simulation is stopped once the cylinder pressure reaches the designated discharge pressure.

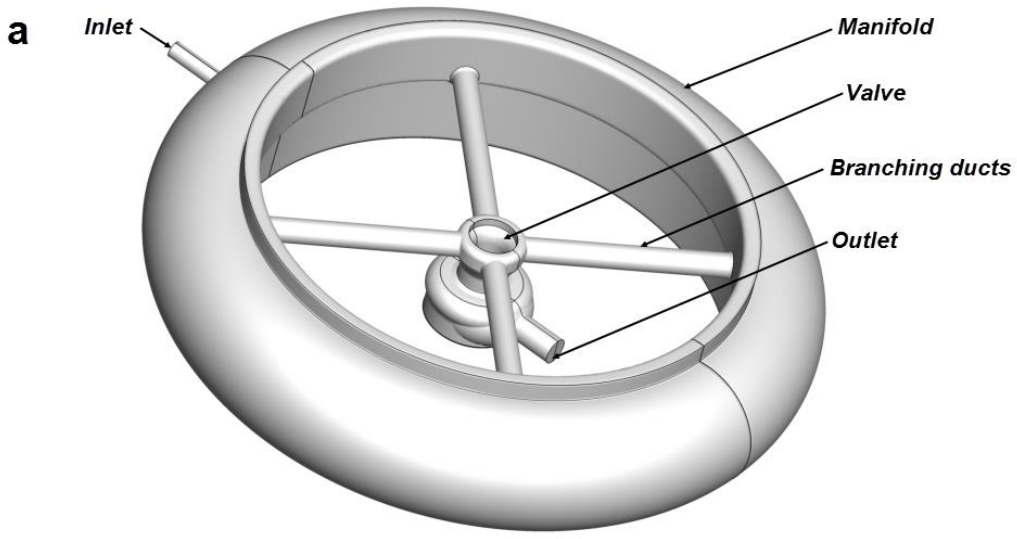

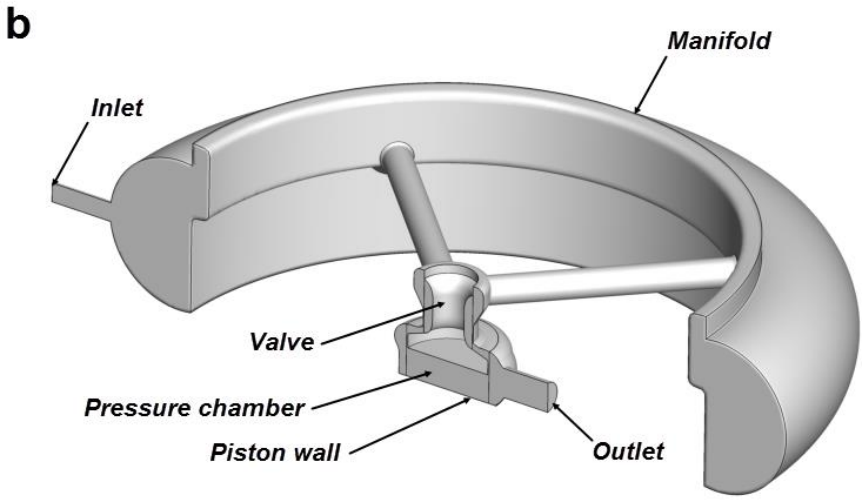

Fig. 1 (a) Full and (b) section view of the fluid volume inside the pump, showing the main pump components.

In the actual mechanical configuration, the valve on top of the pressure cylinder moves due to the pressure and spring forces acting on it; however, in order to simplify the simulation, the valve was assumed to move following a prescribed motion, estimated through simplified 1-D analysis performed by an industrial partner, which provided the profile shown in **Fig. 2**. Likewise, a sinusoidal movement profile was imposed for the movement of the plunger to replicate the force of the crankshaft. An additional line is evident on the graph of **Fig. 2** referred to as "limited valve motion", since the valve movement had to be limited to a minimum lift of 75 μm for purely numerical (grid-topology) purposes. The "closing" of the valve was accomplished with a special treatment of the boundary condition at the interface, as will be discussed in greater detail in the following section.

A cycle of pump operation commences with the downward movement of the plunger, while the valve is kept closed, thus resulting to the liquid expansion within the cylinder volume. At $2.6 \cdot 10^{-3}$ s, the valve opens signifying the start of the suction period, where fuel enters inside the chamber. The valve closes once again at $5.4 \cdot 10^{-3}$ s, while the piston reaches its lower dead-centre point at

$6.24 \cdot 10^{-3}$ s and subsequently starts its ascending motion. From 6.2 to $8.9 \cdot 10^{-3}$ s the valve is open with the piston moving upwards and hence surplus liquid is pushed towards the manifold. At approximately $8.9 \cdot 10^{-3}$ s the valve seals the chamber, and the last part of the pump-stroke simulation is characterized by the constant liquid pressurization up to $2000 \cdot 10^{5}$ Pa. In the real application, at that pressure, the pressurized fuel unseats the outlet check valve and enters the common rail system.

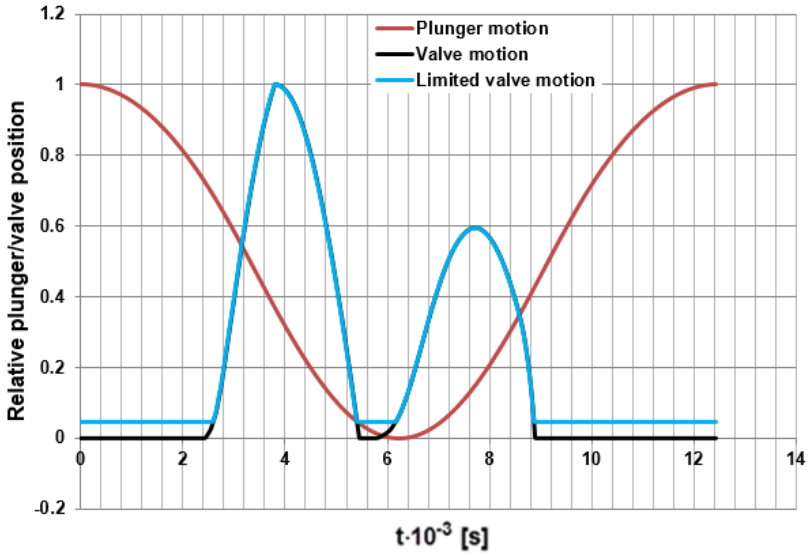

Fig. 2 The pump plunger and valve motion profiles (normalized by the maximum displacement in each case).

3. Numerical methodology

In order to resolve the flow inside the pump, it is necessary to discretize the fluid volume in a set of computational elements over which the conservation equations are solved. By taking advantage of the existing symmetry, the computational domain was truncated to half the original geometrical layout (see **Fig. 1b**), in order to decrease the computational cost. The multiphase, cavitating flow inside the pump was simulated using an implicit, pressure-based solver, Fluent v.16[24]. The govern-

ing equations comprised the continuity and momentum equations, while the energy equation was omitted due to the fact that the Jakob number $Ja = \rho_l c_{p,l}(T_l - T_{sat}) \Big/ \rho_v h_{fg}$ obtains very high values in the order of hundreds in the regions of phase change and thus it can be deduced that mass-transfer within the pump is exclusively designated by inertial forces[17].

Turbulence effects were accounted for with the k-omega SST model, as the Reynolds number can reach values up to 38000 depending on the phase of the operation cycle and the characteristic length scale of each specific sub-volume. Since there is evidence[25,26] in the literature that turbulence has an influence on cavitation structures and, moreover, that it is not always possible this interaction to be captured with traditional RANS models, the SAS variant, capable of capturing the larger transient turbulent structures, has been employed[27]. Cavitation was modelled with the use of a novel barotropic, Homogenous Equilibrium Model (HEM), implemented in the solver as a User Defined Function (UDF). The model aims to replicate phase change without introducing an additional PDE for vapour fraction transport, since mass-transfer rate is considered infinite and consequently density is linked directly to pressure. It was deemed preferable to develop a novel phase-change model instead of employing the bubble dynamics models available in Fluent for reasons concerning both numerical robustness and accuracy of cavitation-erosion prediction. The HEM model solves only the continuity & momentum equations[28], since pressure is directly linked to density. A vapour advection equation is redundant, which speeds up calculations and grants additional robustness. Besides, the barotropic model is capable of predicting the Rayleigh collapse of vapour structures inherently, contrary to two-phase, mass-transfer models, making it suitable for erosion prediction[29,30]. It must also be pointed out that bubble-dynamics models are, in essence, problem-specific and require tuning through semi-empirical parameters. On the contrary, barotropic models do not need such tuning, while they rely on the thermodynamic-equilibrium assumption, which has been demonstrated in experiments to be valid[31].

According to the formulation of the HEM, an appropriate equation of state (EoS) is required that corresponds to the phase change of the liquid to the liquid/vapour mixture. In this work, the influence of thermal effects has been omitted given the fact that Diesel temperature and thus, vapour pressure increase is very small[32], in respect to extreme pressurization (i.e. $2000 \cdot 10^5$ Pa), much higher than the pressure prevailing in the pump chamber for the entire flow time apart from the very last time-steps where all cavitation has already collapsed. Such an approximation is often employed in the simulation of cavitating flows in engineering applications[33,34] and, in conjunction, to the objective of tracking erosion-formation probability, the use of the barotropic model is justified. Hence, a piecewise EoS was used, based on the following component functions (see also[33,35]):

- the Tait EoS was used for the liquid phase:

$$p(\rho) = B\left[\left(\frac{\rho}{\rho_l}\right)^n - 1\right] + p_{sat,l} \qquad \rho \geq \rho_l \tag{1a}$$

where the factor B corresponds to the bulk modulus of the liquid and n is an exponent determining the stiffness of the Tait EoS, commonly set to 7.15 for weakly compressible liquids[22]. The density predicted by the Tait EoS was tested and found to be in good agreement with the literature data for Diesel fuel[32], for the temperature level and the pressure range in the pump. In fact, the maximum error is less than 0.7% for pressures up to $2000 \cdot 10^5$ Pa, which is considered negligible.

-the isentropic-gas EoS was used for the gas phase:

$$p(\rho) = C\rho^{\gamma} \qquad \rho \leq \rho_v \tag{1b}$$

where C and γ are the constant of the isentropic process and the heat capacity ratio, respectively.

- an EoS based on the Wallis speed-of-sound formula was employed for the mixture:

$$p(\rho)=\frac{c_v^2 c_l^2 \rho_v \rho_l (\rho_v-\rho_l)}{c_v^2\rho_v^2-c_l^2\rho_l^2} ln\left(\frac{\rho}{c_l^2\rho_l(\rho_l-\rho)+c_v^2\rho_v(\rho-\rho_v)}\right)+p_{ref} \quad \rho_v \le \rho \le \rho_l \tag{1c}$$

where c is the speed-of-sound velocity, the variation of which depending on the mixture density is depicted in Fig. 3. ρ corresponds to density, while the subscripts l and v refer to the liquid and vapour phases, respectively. It is essential to mention that p_{ref} and $p_{sat,l}$ on the right-hand side of Eqs. (1a) and (1c) are reference values in order to ensure that the pressure is a continuous function of density at the limits of ρ_l and ρ_v. Besides, if the formulation of Eq. (1) is considered, it becomes obvious that there is a small pressure difference equal to $\Delta p = p_{sat,l} - p_{sat,v}$ during the phase change. In practice, this difference is small compared to the pressure levels prevailing in the simulation. The variation of pressure with density covering the entire range from pure liquid to pure vapour is also depicted in **Fig. 3**. The thermophysical properties of the liquid (l) and vapour (v) phases used in this study correspond to a temperature of 318 K and are summarized in **Table 1**. The values were obtained from the database provided by Kolev[32].

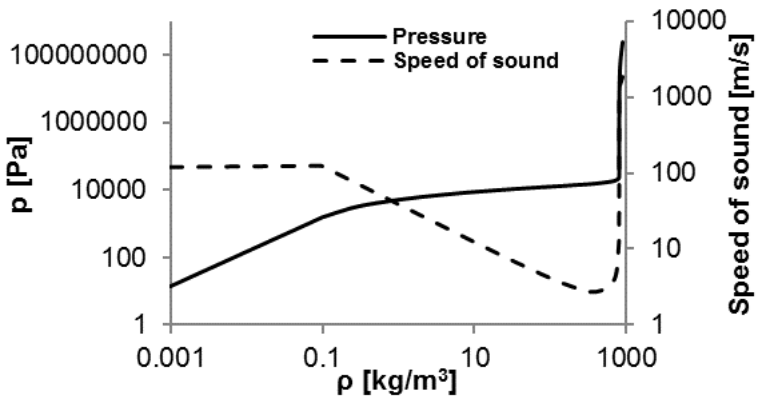

Fig. 3 Pressure variation with density as produced the barotropic HEM EoS and respective variation of the speed of sound.

Table 1 Thermodynamic properties for diesel, liquid and vapour at 318K[32].

Liquid properties			Vapour properties		
B	$207.1 \cdot 10^6$	Pa	C	16227.7	$Pa/(kg/m^3)^{\gamma}$
n	7.15	(-)	γ	1.02	(-)
$\rho_{sat,l}$	811.6	kg/m^3	$\rho_{sat,v}$	0.098	kg/m^3
$c_{sat,l}$	1350.6	m/s	$c_{sat,v}$	125.8	m/s
$p_{sat,l}$	36901.3	Pa	$p_{sat,v}$	1524.8	Pa
μ_l	$2.13 \cdot 10^{-3}$	Pa·s	μ_v	$8 \cdot 10^{-6}$	Pa·s

Appropriate boundary conditions were imposed for the governing equations in accordance to the real flow conditions prevailing within the pump layout. A uniform pressure profile of $6.5 \cdot 10^5$ Pa was imposed at the pump inlet:

Inlet: $p=p_{in}=6.5 \cdot 10^5$ Pa (2)

while, as has been already mentioned, a wall was placed at the pump outlet. The no-slip condition was applied on all fluid-wall interfaces:

Outer surfaces: $\boldsymbol{u}=0$ (3)

Besides, continuity of the velocity components, was imposed at the interfaces between the different fluid sub-domains, which are depicted in different colours in **Fig. 5**. Special treatment of the boundary conditions was required during the discrete phases (suction or pressurization) of the pump operation. Once the valve was considered fully closed the interfaces corresponding to the clearance of 75 μm between the valve and valve seat, also indicated in **Fig. 5**, were switched to walls to prevent liquid from flowing into the chamber. On the contrary, when the valve lift was assigned values larger than 75 μm topology the interfaces were switched to a permeable condition. More specifical-

ly the boundary condition placed depending on the respective phase of pump operation was as follows:

$$\text{Needle/needle-seat interface:} \quad \begin{cases} \boldsymbol{u}\big|_{\text{int}} = 0 & 0 \le t < 2.6\cdot10^{-3}\ s,\ 5.4\cdot10^{-3}\ s \le t < 6.2\cdot10^{-3}\ s,\ t > 8.9\cdot10^{-3}\ s \\ \boldsymbol{u}\big|_{int,-} = \boldsymbol{u}\big|_{int,+} & 2.6\cdot10^{-3}\ s \le t < 5.4\cdot10^{-3}\ s,\ 6.2 \le t < 8.9\cdot10^{-3}\ s \end{cases} \tag{4}$$

The governing equations, i.e. the continuity and momentum equations[28] for a single fluid, along with the boundary conditions were solved using a coupled pressure/velocity solver, in order to maximize stability of the solution. A body-force weighted scheme was employed[36] for pressure interpolation, while second-order accurate upwind schemes were used for momentum, density and turbulence advection. Progression in time was performed with a first-order implicit method, so as to avoid issues of numerical instability due to time-step selection. A time step of 1 μs was chosen for the simulations that, based on the domain discretization, corresponded to a Courant number in the order of 15, which could be well handled by the implicit solver.

3.2 Validation studies

The validity of the formulated HEM has been verified considering a benchmark shock tube test-case, as discussed in detail in[35]. It has been demonstrated that the solution produced by the barotropic model is in excellent agreement with the exact solution of the Riemann problem with the barotropic equation of state[37] and therefore that the pressure-based solver is able to replicate the correct pressure wave pattern. Furthermore, the predictions of the HEM have been compared against the respective produced by two-phase, bubble dynamics models and experimental data available for a square-throttle configuration and were verified to be in good agreement, as reported in[33].

A further validation study was conducted in this study in a shock-tube configuration, which, however, bears some resemblance to the actual geometry in the sense that phase-change occurs due to the wall displacement at the tube right end with a velocity of 3m/s. The left-side end is kept at a constant pressure of $6.5 \cdot 10^5$ Pa, which is also equal to the pump inlet pressure. The solution at a time instance of $1.0 \cdot 10^{-3}$ s is shown on **Fig. 4**, along with a reference solution, which can be found in[38]. As can be seen, regarding both the velocity (**Fig. 4a**) and density (**Fig. 4b**) distributions along the tube length good agreement is achieved between the numerical and reference solutions.

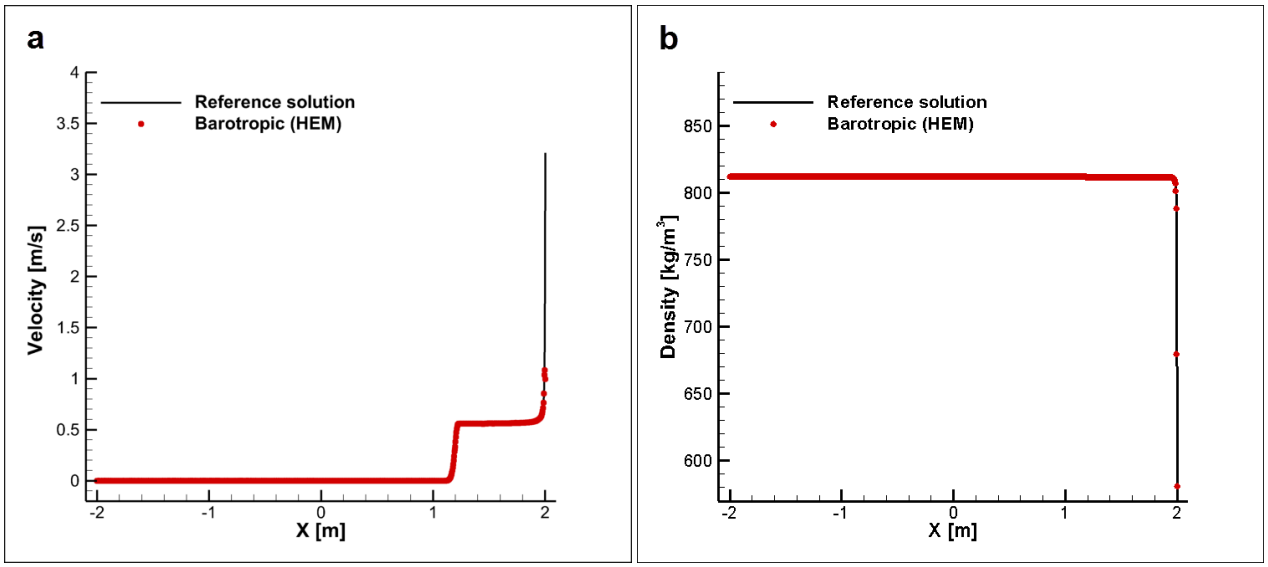

Fig. 4 Shock-tube case with moving wall: (a) velocity and (b) density distributions at $t=1.0 \cdot 10^{-3}$ s.

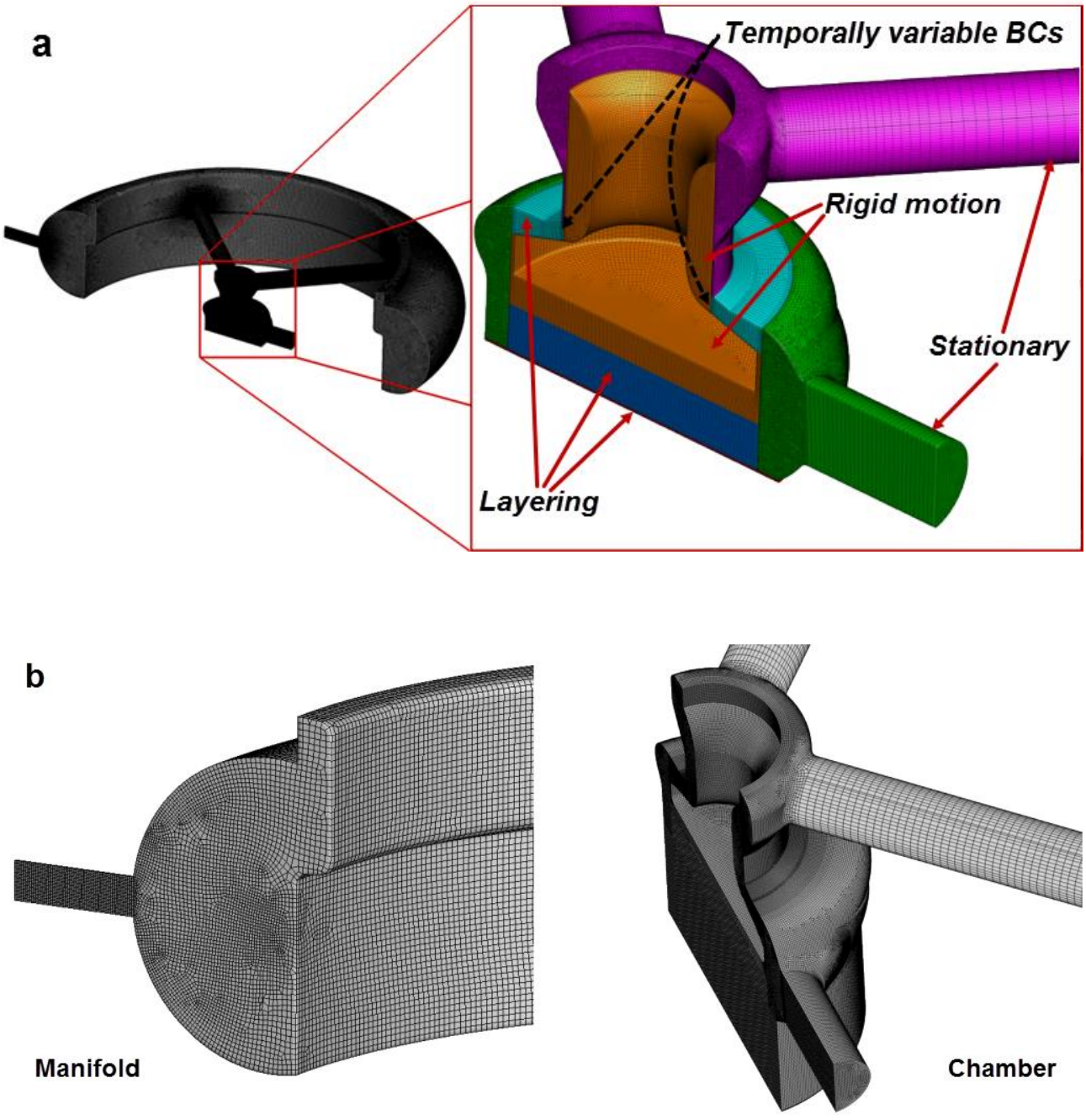

Fig. 5 (a) Moving-mesh technique applied on the different volumes comprising the domain and (b) detail of the hexahedral-core mesh consisting of 1.2-million elements.

3.1 Grid motion and independence

The grid employed for the discretization of the computational domain was constructed by partitioning the original geometry in several simpler volumes, as shown in **Fig. 5**. Moreover, in order to accommodate the mesh motion of each moving sub-domain it was necessary to split the individual volumes as well and use non-conformal interfaces to connect them. However, conformal grids were adapted between adjacent static volumes. The computational mesh was structured is such a way to accommodate the valve and piston motion with the method of layering, namely splitting (or respectively merging) of the grid elements when their height-to-width ratio becomes larger (or respectively smaller) than a predefined value. Element layers were added, or subtracted depending on the movement of the valve and the piston, on the upper and lower surfaces of the cylinder, as also indicated in **Fig. 5**. Grid refinement was performed in the regions of interest of small length scale where complex flow topology was also expected to occur; for example, elements with an edge length of 0.4 mm and 0.1 mm, respectively, were placed in the manifold and pressure chamber, respectively.

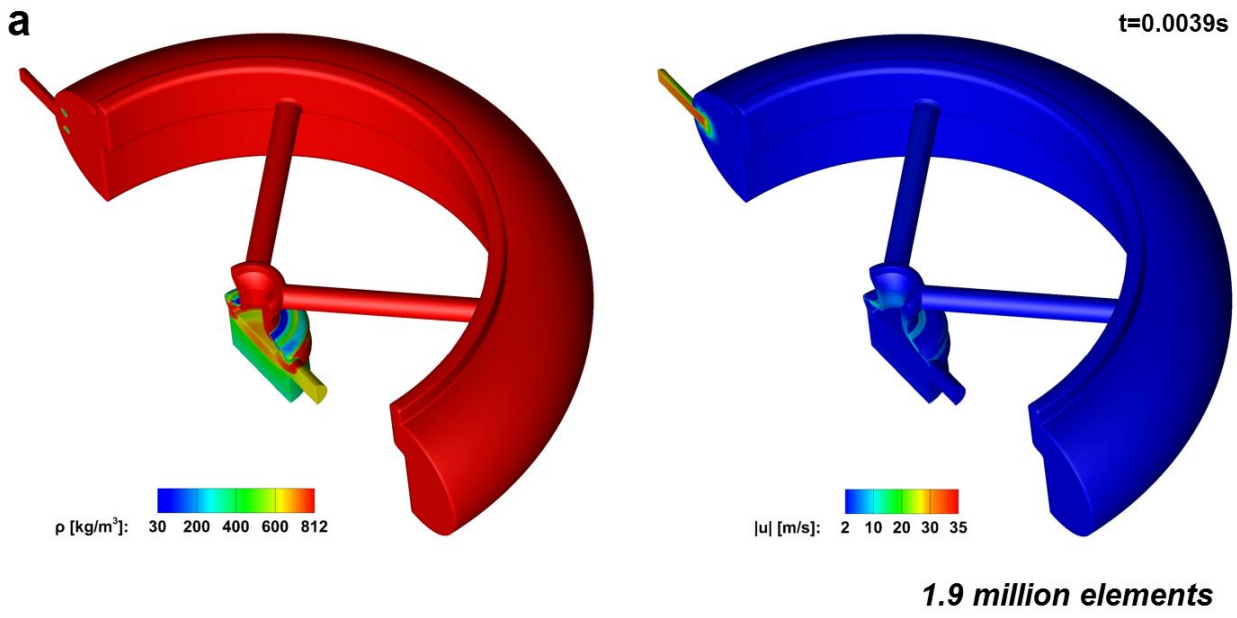

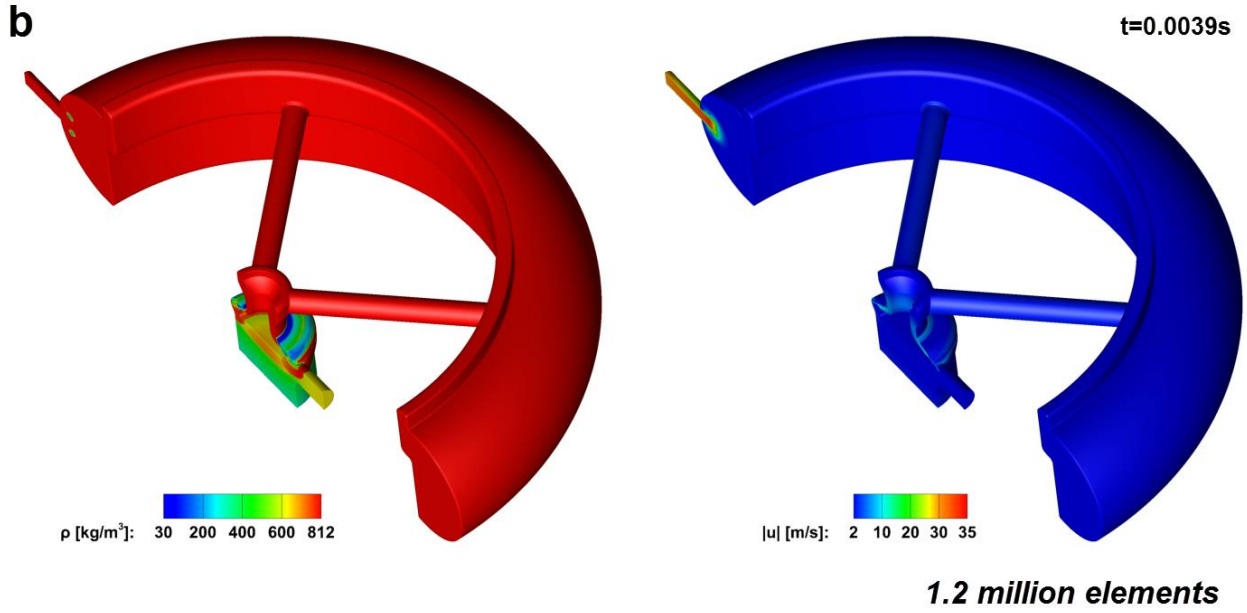

Fig. 6 The velocity and density fields as predicted using the (a) 1.9-million and (b) 1.2-million grids.

Grids of different topology and element count have been tested to verify the independence of the solution from the grid density. More specifically, a grid comprising $1.9 \cdot 10^6$ elements, depicted in **Fig. 5a**, was initially tested, where non-axisymmetric volumes (e.g the manifold) were discretized using an unstructured mesh exclusively comprising tetrahedral elements. A further effort was made to reduce the overall number of grid elements and thus the computational cost by applying a hexahedral core mesh, shown in **Fig. 5b,** to discretize the manifold (and other regions such as the stationary part of the pressure chamber). It was made possible the overall cell count in the manifold region to be reduced to 340000 elements instead of $1.1 \cdot 10^6$, which allowed a further grid refinement to be performed in the chamber region (824000 instead of 558000 elements). The second grid comprised $1.2 \cdot 10^6$ elements in total.

The velocity and density fields at a time instance of $3.4 \cdot 10^{-3}$ s, as predicted by both grids are presented in **Fig. 6**. It is evident that the solutions produced by the two grids both fields are indistin-

guishable demonstrating independence from the grid density. Besides, the discrepancy in the minimum liquid volume fraction predicted by the two models at the time instance of $6.2 \cdot 10^{-3}$ s is less than 1%. Hence, the grid comprising $1.2 \cdot 10^{6}$ elements was employed for the production of the results presented in section 4.

3.3 Specification of areas susceptible to cavitation erosion

The methodology taken into consideration for the prediction of probable erosion sites is based on the concept of an adverse pressure gradient serving as the necessary cause for the collapse of cavitation structures. Two pre-requisite conditions must be met for a location to be characterized as susceptible to cavitation-induced erosion:

$$\frac{da}{dt} < 0 \tag{5}$$

$$\frac{dp}{dt} < 0 \tag{6}$$

According to Eq. (5), during the cavitation-collapse stage, the overall volume of the vapour cloud must be decreasing, as indicated by the negative gradient the of the volume fraction total derivative, defined as:

$$\frac{da}{dt} = \frac{\partial a}{\partial t} + \boldsymbol{u} \cdot \nabla a \tag{7}$$

Likewise, Eq. (6) implies that a steeper pressure gradient leads to more violent collapse of the vapour structures. The use of the total instead of the partial derivatives as indicators of cavitation aggressiveness constitutes a generalized method and is based on the fact that bubbles at the final collapse stages follow the streamlines. Hence, use of total derivatives constitutes the indicators applicable to both quasi-steady and unsteady flows. The quantities indicative of erosion susceptibility, i.e. *da/dt* and *dp/dt*, were coded as UDFs, calculated at each time-step and averaged over the entire flow time. Besides, the peak-pressure values occurring during the collapse of vapour structures have also been recorded, as the locations where these values are detected also signify sites prone to erosion.

4. Results

The numerical predictions of the two-phase flow inside the investigated configuration, as produced by the homogeneous equilibrium model are analysed in this section. Selected instances of the simulated pumping cycle are shown, suitable for elucidating the development and topology of the cavitating flow arising within the geometrical layout during the various stages of the pump operation. First of all, contour plots of the instantaneous pressure field at several time instances of the operating cycle are presented in **Fig. 7**. As expected, at the first stages of the cycle ($t < 2.6 \cdot 10^{-3}$ s), while the valve is still closed, pressure drops inside the cylinder only, whereas the manifold remains at the inlet pressure of $6.5 \cdot 10^{5}$ Pa ($t=0.1 \cdot 10^{-3}$ s). After the opening of the valve, which occurs at $t=2.6 \cdot 10^{-3}$ s, a rarefaction wave travels upstream toward the inlet and fuel flows inside the manifold and consequently the cylinder. Successive regions of low and high pressures are evident in the vicinity of the inlet (see instance at $t=3.9 \cdot 10^{-3}$ s), which are associated with the formation of a jet en-

tering the manifold, as will be discussed in further detail in the next paragraph. Once the valve closes for a second time, high pressures can be detected in the region upstream of it (see instance at 5.4ms); this effect has been well-documented in the literature and termed as 'water hammer effect'[39], caused due to the fluid deceleration in that region. Finally, the valve opens again at $6.2 \cdot 10^{-3}$ s and all the flow processes already mentioned are repeated. The propagation of the rarefaction wave, caused by the second valve opening, travelling toward the pump inlet is illustrated by the plot at the time instance of $7.2 \cdot 10^{-3}$ s. Besides, it must be pointed out that, although the piston is reducing the cylinder volume during the second valve opening, pressure in the cylinder is still low even at 8.8ms (**Fig. 7**), probably due to the existence of vaporous structures. Actually, the liquid pressurization within the chamber commences after a time period of $9.2 \cdot 10^{-3}$ s.

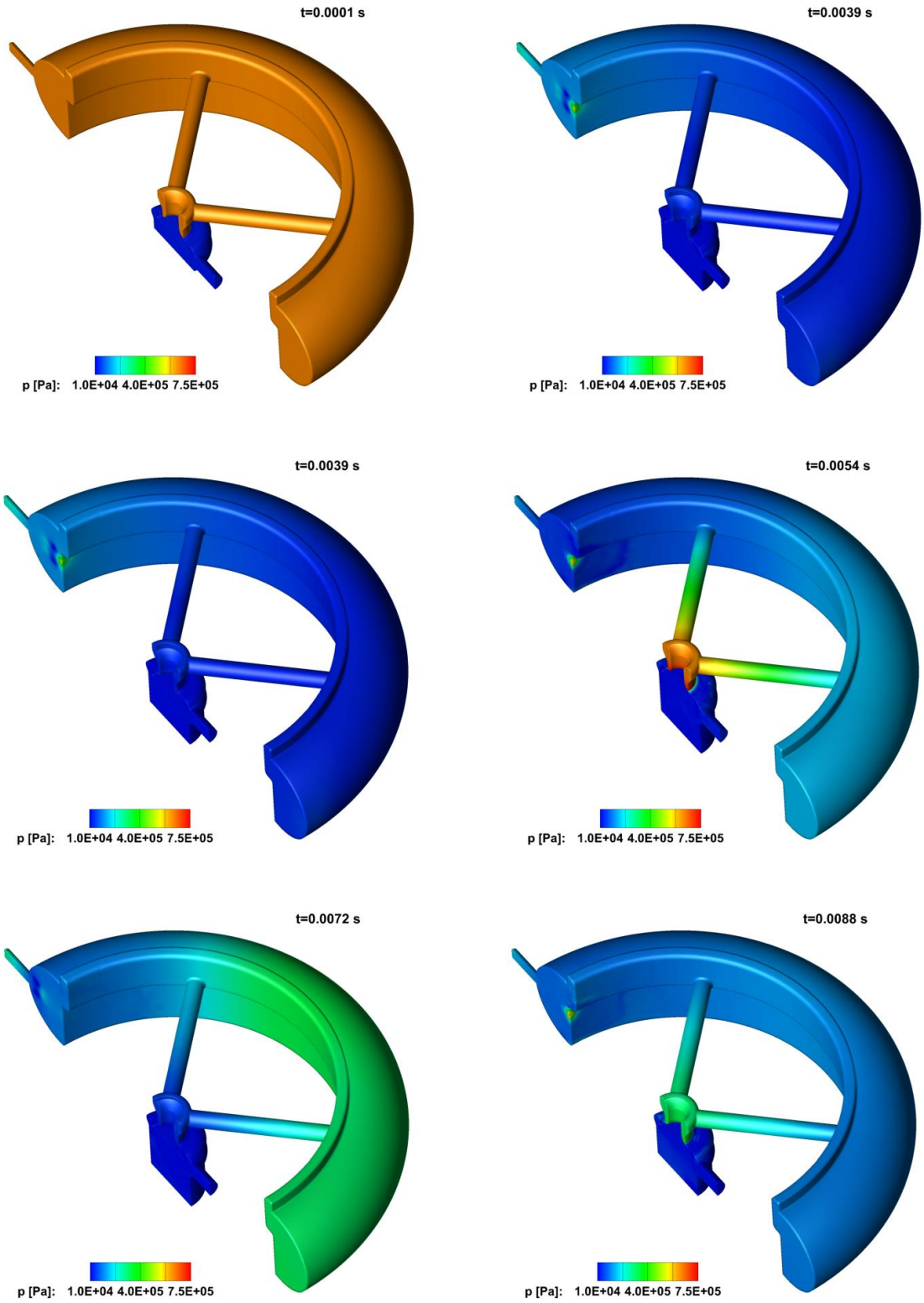

Fig. 7 Contour plots of the pressure field at different time instances, as calculated by the barotropic model (HEM).

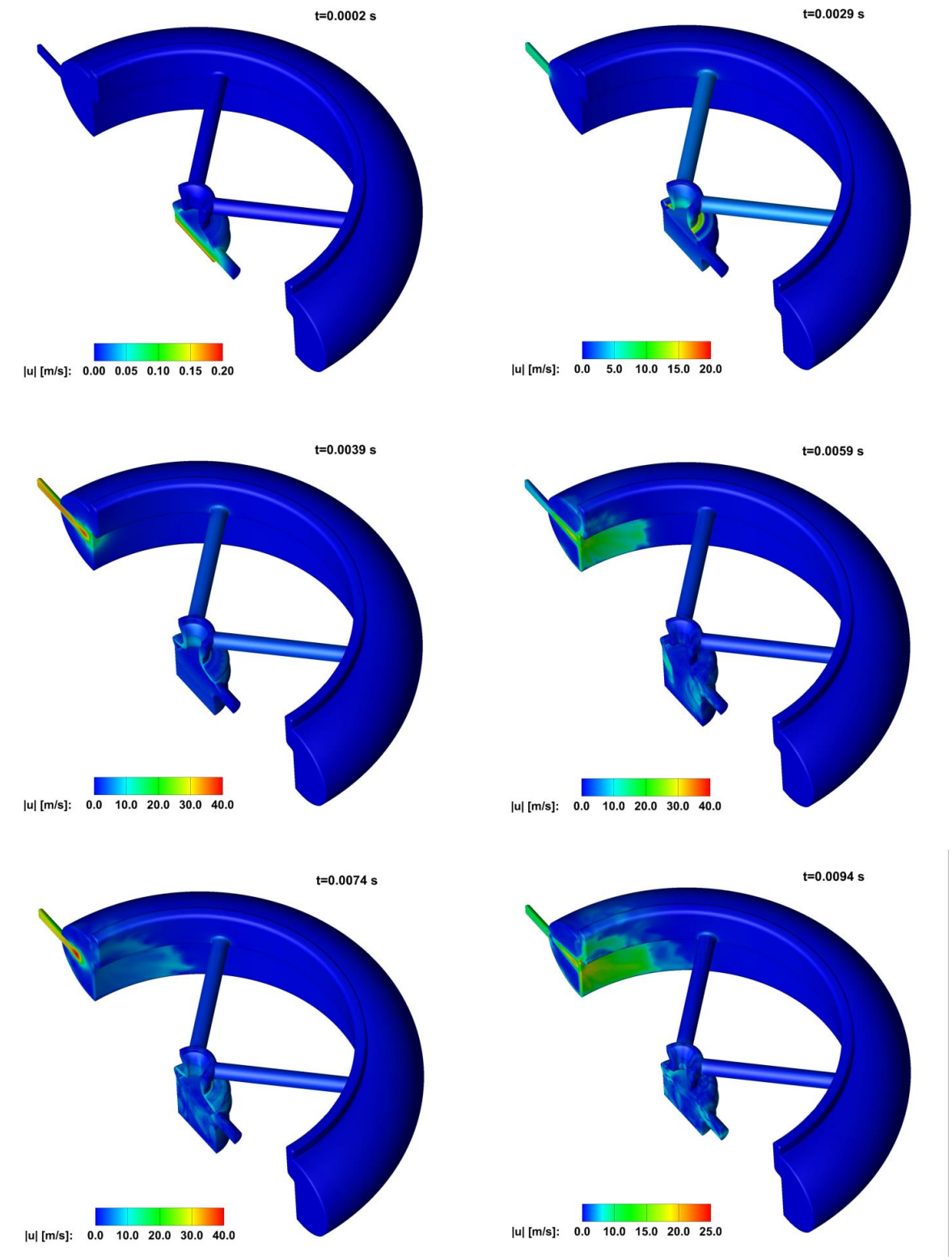

Fig. 8 Contour plots of the velocity-magnitude field at different time instances, as calculated by the barotropic model (HEM).

Referring to the velocity field (**Fig. 8**), it is obvious that prior to the valve opening fluid flow occurs only within the chamber with velocities of small magnitude (see instance at $t=2.0\cdot10^{-3}$ s). Once the valve opens, liquid enters the manifold and consequently the cylinder, while high velocities in the order of 19 m/s being detected (at the instance of t=2.9 m/s) in the gap between the valve and valve seat due to the throttling effect imposed by the geometrical constriction. Besides, as made evident by the contour plot at $t=3.9\cdot10^{-3}$ s, a fuel jet is formed from the inlet duct into the manifold volume. The jet impinges on the opposite wall creating the stagnation point evident in **Fig. 7** (see respective plot at $t=3.9\cdot10^{-3}$ s) and spreads radially ($t=5.9\cdot10^{-3}$ s), however the liquid is impeded from flowing further downstream into the manifold due to the existence of a pressure wave (see **Fig. 7** at $t=5.4\cdot10^{-3}$ s). In addition, the low flow velocities at the region between the valve and valve seat illustrated by the plot at $t=5.9\cdot10^{-3}$ s are indicative of the water-hammer effect discussed in the previous paragraph. At $t=7.4\cdot10^{-3}$ s after the start of the operating cycle, the valve is open and the respective plot of **Fig. 8** reveals the formation of an additional fuel jet, as the flow phenomena exhibit a repetitive trend.

Two characteristic time instances have been selected in order to elucidate the complex flow pattern that manifests in the cylinder. More specifically, iso-surfaces of the second invariant of the velocity gradient tensor, also known as the "Q criterion", suitable for identifying vortical structures[40] are plotted for t=5.9 and $7.2\cdot10^{-3}$ s and presented in **Fig. 9**. The iso-surfaces were coloured according to the local vorticity magnitude, while iso-surfaces of the vapour volume fraction (a=0.25) are also plotted in **Fig. 9** to give an indication of the respective phase field. It is evident that numerous structures exist on the upper part of the chamber closer to the valve tip, with the ones with the highest vorticity-magnitude values being located at the clearance between the valve and its seat. A closer look at the plot also reveals that more structures can be detected on the chamber side close to the

outlet duct with vortices entering the duct as well (**Fig. 9a**). The vortical structures appear to have diminished in magnitude at $7.2 \cdot 10^{-3}$ s (**Fig. 9b**), however once again the topology is asymmetrical with more structures towards the outlet duct.

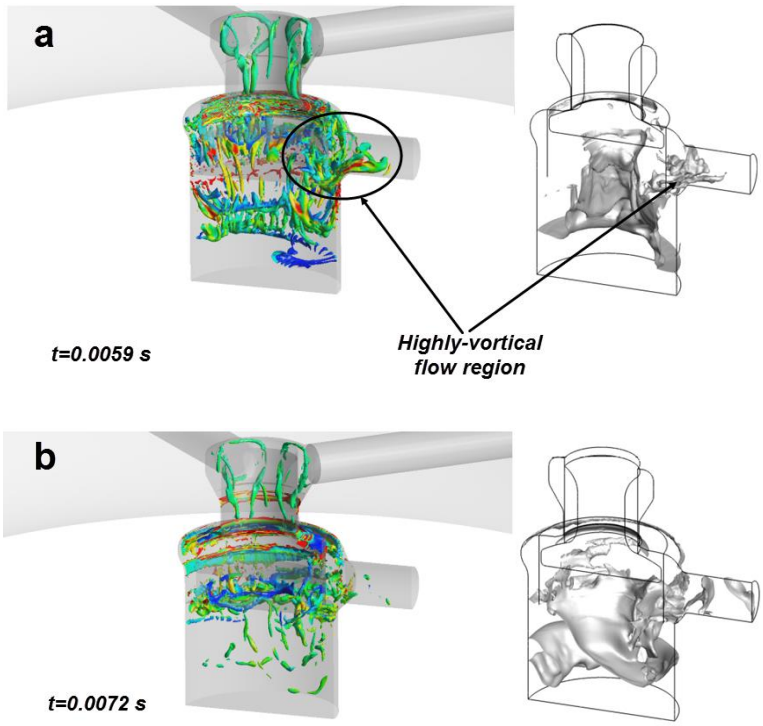

Fig. 9 Iso-surfaces of the second invariant of the velocity-gradient tensor ($Q=2 \cdot 10^{7}$ s^{-2}) and of the vapour volume fraction (a=0.25) at different time instances. The Q iso-surfaces are coloured with vorticity-magnitude values in the range 0–25000 s^{-1} (blue-red): (a) t=0.0059s and (b) t=0.0072s

The emergence of cavitation inside the pump geometry is illustrated through contour plots of the density field presented in **Fig. 10**. As expected, the depressurization of the chamber at the first stages of operation causes the fuel to cavitate, thus a mixture of liquid and vapour forms, with the lowest density detected at the vicinity of the moving piston wall (see plot at $t=0.2 \cdot 10^{-3}$ s). After the valve opening(see plot at t=3.9ms), the acceleration of the fuel in the vicinity of the valve passage and the low pressures prevailing in that region cause further vapour formation, with the density locally reaching values as low as 48 kg/m^3.

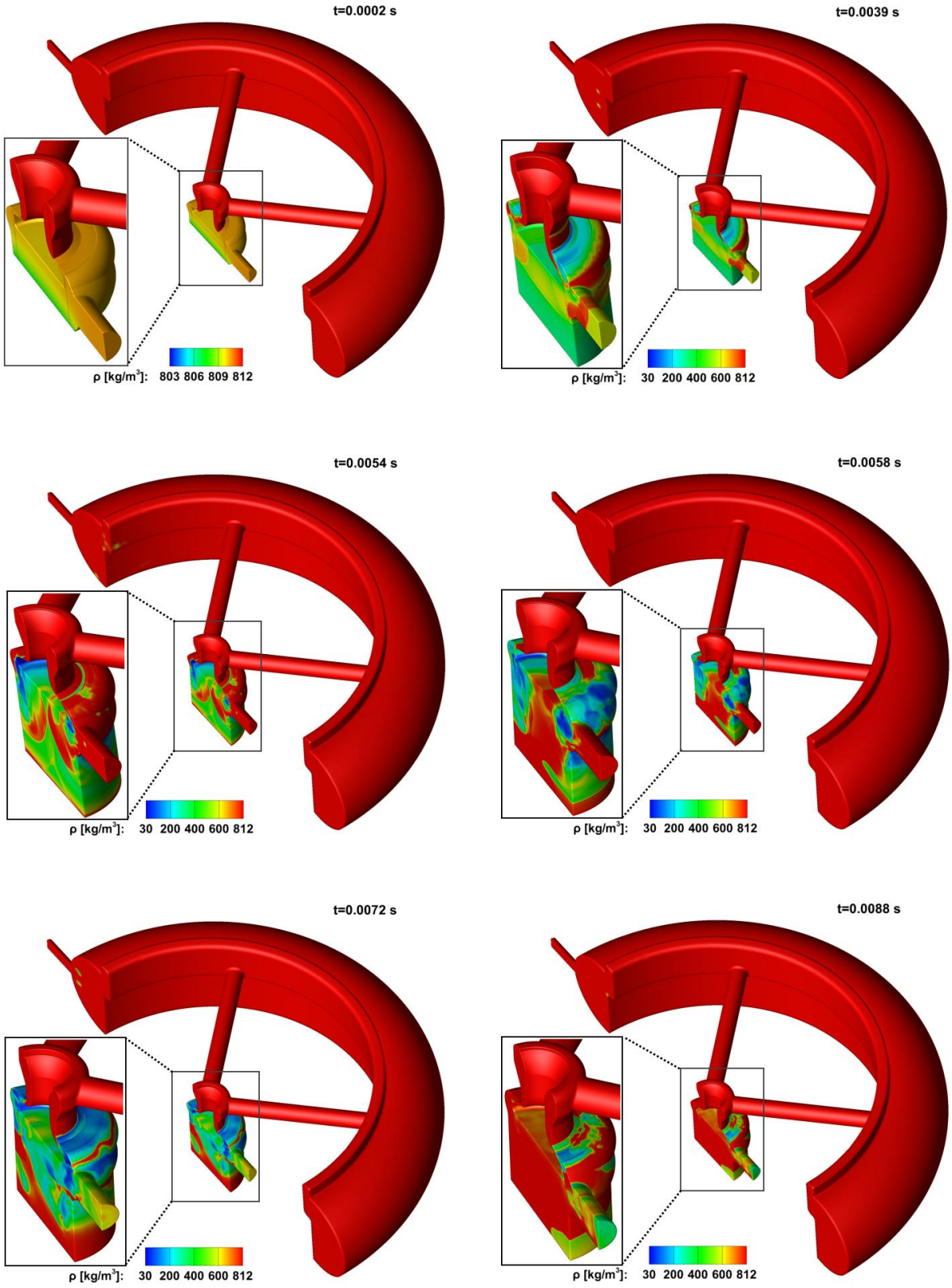

Fig. 10 Contour plots of the density field at different time instances, as calculated by the barotropic model (HEM).

Another notable feature characterizing the pump suction phase is the formation of cavitation rings that collapse on the manifold wall opposite of the inlet duct. These vaporous structures set in due to the low-pressure regions existing on each side of the fuel jet that enters the manifold volume (see also **Fig. 7** at $t=3.9\cdot10^{-3}$ s) and are in fact cavitating vortices attributed to the shear flow induced by the jet penetration into the manifold volume. At the time instances of 5.4 and $5.8\cdot10^{-3}$ s, vaporous structures still occupy a significant part of the cylindrical chamber since the downward displacement of the piston is still forcing the liquid in the cylinder to expand. The cavitation topology is designated by the complex flow field arising within the cylinder.

Cavitation structures still persist at $7.2\cdot10^{-3}$ s, although the piston is moving upwards, due to the second opening of the valve. However, the lower part of the chamber is mainly occupied by pure liquid. If the respective plot of the pressure field (**Fig. 7**) is considered, illustrating values close to saturation in the cylinder, it can be easily deduced that the volume reduction of the cylinder is absorbed by the vapour collapse, thus the pressure does not rise above saturation. Finally, at $t=8.8\cdot10^{-3}$ s, where the valve closes and the pressurization stage commences, some scattered cavitation structures still persist near the piston, around the valve and close to the exit of the outlet duct. It has been verified that cavitation has been totally eliminated after $9.2\cdot10^{-3}$ s of the operating cycle.

The variation of the liquid volume and liquid volume fraction inside the pump cylinder is depicted in **Fig. 11**. It must be noted that the barotropic model gives a density field ρ that describes the two-phase flow. The liquid-phase volume fraction a_l can be then calculated as follows:

$$a_l = \frac{\rho - \rho_v}{\rho_l - \rho_v} \tag{5}$$

where the indices l, v correspond to the liquid and vapour phases. Subsequently, the chamber volume occupied by liquid V_l is estimated as:

$$V_l = a_l \cdot V_c \tag{6}$$

where V_c is the overall chamber volume. It is interesting to notice in **Fig. 11a** that in the phases of operation where the valve is closed, the amount of fuel inside the cylinder is conserved to machine precision, indicating the simulation validity. As illustrated by **Fig. 11b**, the liquid fraction within the cylinder decreases rapidly approximately to 70% in the first stages of the cycle up to $2.6 \cdot 10^{-3}$ s, where the chamber volume expands, while the valve is kept closed. Constant liquid fraction values in the order of 60% are maintained in the time period between successive valve openings ($2.6 \cdot 10^{-3}$ s $< t < 6.2 \cdot 10^{-3}$ s), while, as expected, the liquid fraction increases afterwards, since the liquid is compressed. The minimum predicted liquid volume fraction is approximately equal to 58%, a value that has been confirmed by actual observations of industrial partners, since it was found that at part load conditions the pump delivers liquid of approximately half the swept volume.

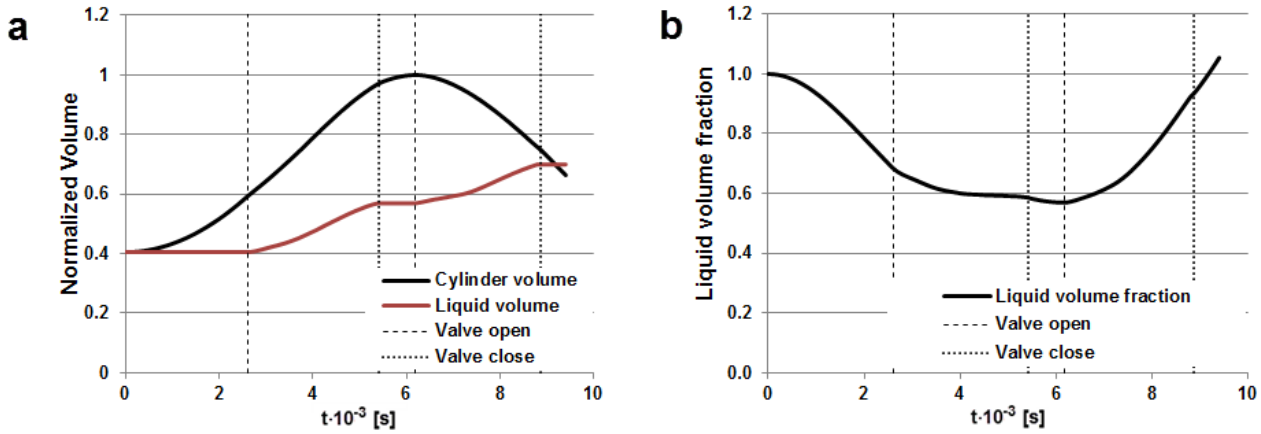

Fig. 11 Variation of (a) the normalized liquid volume and (b) the liquid volume fraction inside the cylinder.

The locations of the pump geometrical layout exhibiting a high risk of erosion are highlighted through **Fig. 12**, which depicts contour plots of the indices employed to pinpoint possible sites of

cavitation-induced erosion. The accumulated pressure-peak distribution for the total simulated flow time is shown in **Fig. 12a**. As can be seen, three distinct locations of high pressure peaks reaching up to $2 \cdot 10^7$ Pa can be discerned, namely the upper surface of the valve tip, the duct wall and the piston edge, with all areas being on the side closer to the outlet. The averaged pressure gradient over the simulation flow time (**Fig. 12b**) also indicates high values in the valve/valve set region and the piston edge. Additional localized spots can be detected on the upper part of the outlet-duct wall close to its mid-length and on the manifold wall opposite to the inlet. Finally, the lowest values of the average volume-fraction gradient (**Fig. 12c**) are detected at the valve-seat wall close to the outlet, while, also, a localized region of low values exists at the manifold wall.

As demonstrated by **Fig. 12**, the valve-tip and valve-seat regions are pointed out as possible erosion sites by all the indices. It has been illustrated by **Fig. 10** that a cavitation cloud establishes in the clearance between the valve and its set due to the flow acceleration imposed by the geometrical constriction. Hence, this cloud collapses close to the solid walls during the compression stage increasing by this way the possibility of erosion development. In fact, the part closer to the pump outlet appears to be more vulnerable since, as shown by **Fig. 10** at $8.8 \cdot 10^{-3}$ s, the cloud collapses asymmetrically. Furthermore, the presence of a vortical, cavitating structure inside the outlet duct (see **Figs. 9** and **10**), which collapses close to the wall, leads to the characterization of that region as erosion-prone. Likewise, the collapse of the cavitating vortices, which emanate due to the fuel-jet penetration into the manifold, on the wall facing the inlet could lead to the onset of erosion at the specific location.

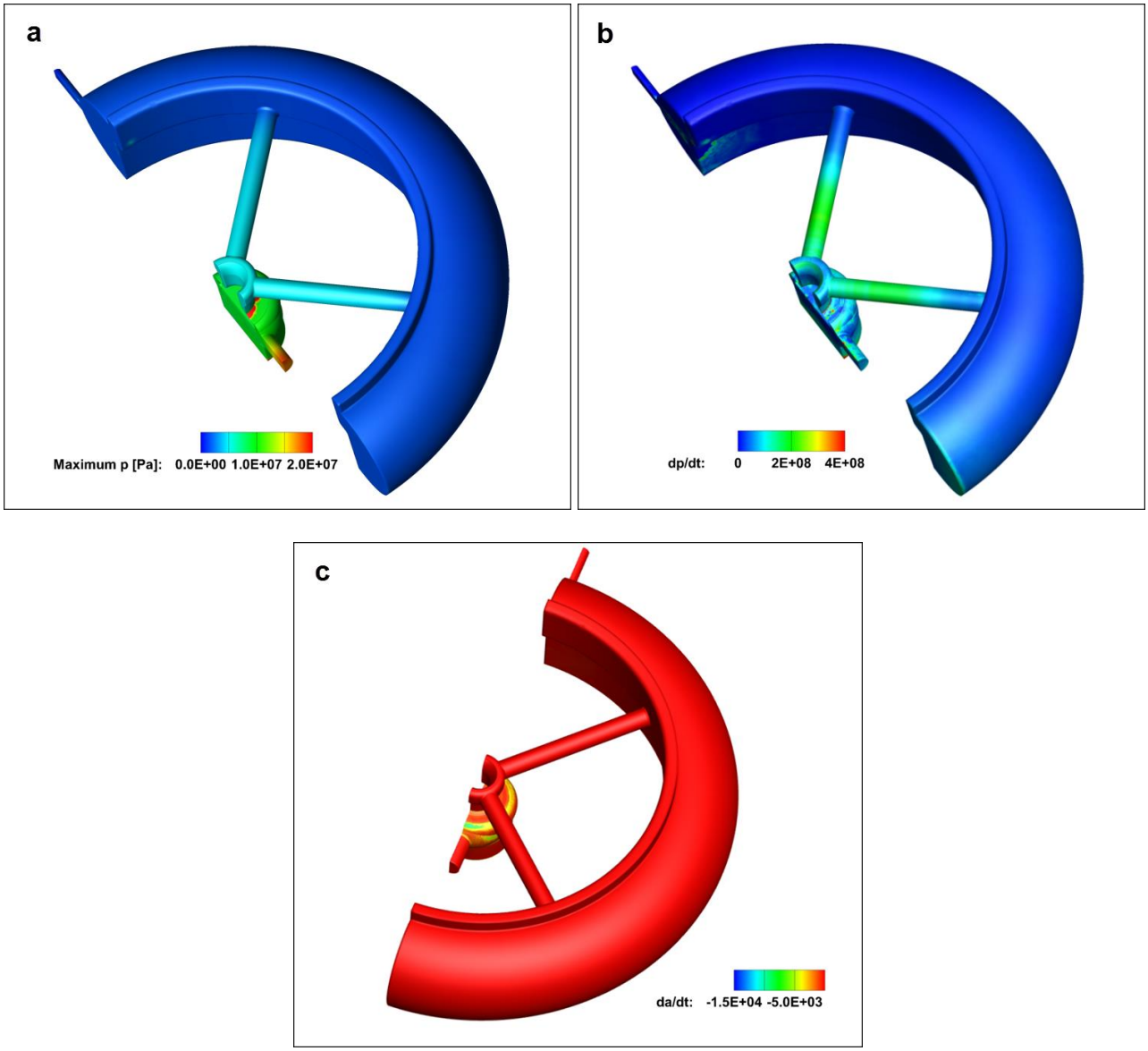

Fig. 12 Contour plots of the cavitation-aggressiveness indicators: (a) accumulated pressure-peak distribution, (b) average pressure gradient and (c) average volume-fraction gradient.

5. Conclusions

The transient operation of a high-pressure, piston-plunger fuel pump was investigated in this study by means of a novel (barotropic) homogeneous equilibrium model (HEM) that has been developed, while also a layering procedure was applied to accommodate the grid modification re-

quired due to the presence of moving elements (piston and valve motion). The model was proven accurate and robust, in fact employing a time step suitable for industrial applications (acoustic courant value of 15). The numerical results demonstrated the onset of cavitation during the pressure-chamber expansion at the early stages of the operating cycle. Opening of the needle further increased the extent of cavitation in the cylinder due to the liquid acceleration in the needle/needle seat geometrical constriction. A vapour/liquid mixture was found to occupy a significant part of the chamber, once the piston reached its lower dead centre. The liquid volume fraction at that specific time instance was calculated approximately equal to 58%, indicating that the pump fuel delivery performance is considerably affected by the formation of cavitation within the compression chamber. Furthermore, the flow field within the cylinder was found to be highly turbulent with numerous vortical structures arising after the valve opening, the action of which has an influence on the cavitation topology leading to an asymmetrical collapse during the compression phase. Before the final collapse of cavitation, localized structures could be detected at three locations, namely at the vicinity of the piston surface, at the gap between the valve/valve seat and at the outlet duct. The eventual collapse of these structures in the vicinity of the solid wall during the compression stage is the cause for the high probability of erosion formation predicted by the cavitation aggressiveness indicators implemented in the solver, i.e. the pressure-peak magnitude, as well as the pressure and volume fraction gradients, in these areas. The valve tip and its seat, the piston edge and the curved outlet wall have been identified as areas susceptible to cavitation-induced erosion. Besides, an additional region at the manifold wall was pointed out as erosion-prone, owing to the collapse of vortical cavitation emerging due the action of the inlet jet entering the manifold and inducing high shear to the stagnant liquid. It can be summarized that the present numerical approach constitutes a valuable computational tool for the characterization of cavitation formation in industrial-scale flows, as well

as possible erosion-related after effects, since it has been able to predict the cavitation collapse and identify erosion-susceptible regions with a reasonable computational cost.

Acknowledgments

The research leading to these results has received funding from the People Programme (IAPP Marie Curie Actions) of the European Union's Seventh Framework Programme FP7/2007-2013/ under REA grant agreement n. 324313. The authors would like to acknowledge the contribution of The Lloyd's Register Foundation. Lloyd's Register Foundation helps to protect life and property by supporting engineering-related education, public engagement and the application of research.

References

1. Catania AE, Ferrari A. Development and performance assessment of the new-generation CF fuel injection system for diesel passenger cars. Appl Energy 2012; 91 483–495.
2. Silva PASF, Shinomiya LD, de Oliveira TF, Vaz JRP, Amarante Mesquita AL, Brasil Junior ACP. Analysis of cavitation for the optimized design of hydrokinetic turbines using BEM. Appl Energy, 2016, In press.
3. Moon S, Huang W, Li Z, Wang and J. End-of-injection fuel dribble of multi-hole diesel injector: Comprehensive investigation of phenomenon and discussion on control strategy. Appl Energy 2016; 179, 7–16.
4. Karlsen-Davies ND, Aggidis GA. Regenerative liquid ring pumps review and advances on design and performance. Appl Energy 2016; 164: 815–825.
5. Avellan F. Introduction to cavitation in hydraulic machinery. In: 6th International Conference on Hydraulic Machinery and Hydrodynamics, Timisoara, Romania, 2004.

6. Schmidt H, Kirschner O, Riedelbauch S. Cavitation measurements on a pump-turbine model. J Phys Conf Ser 2015; 656: 012071.

7. Wang S. The Analysis of Cavitation Problems in the Axial Piston Pump. J Fluids Eng 2010; 132: 074502.

8. Kumar S, Bergada JM. The effect of piston grooves performance in an axial piston pumps via CFD analysis. Int J Mech Sci 2013; 66: 168-179.

9. Ni WW, Bartholme D, Cass M. The CFD Analysis of Pressure Pulsation in the Aircraft Engine and Control Systems Lubrication Pump. SAE Int J Aerosp 2013; 6: 49-55.

10. Frosina E, Napoli U. A Tridimensional CFD Analysis of the Oil Pump of an High Performance Engine. SAE Tech Pap 2014-01-1712.

11. Petzold M, Weber J, Dautry E, Ohligschläger O, Müller A. Visualization and analysis of the multiphase flow in an electromagnetically driven dosing pump, In: ASME/BATH 2013 Symposium on Fluid Power & Motion Control, Florida, USA, 2013.

12. Giuffrida A, Ficarella A, Laforgia D. Study of the delivery behaviour of a pump for common rail fuel injection equipment. Proc Inst Mech Eng Part I J Syst Control Eng 2009; 223: 521-535.

13. Iannetti A, Stickland MT, Dempster WM. An advanced CFD model to study the effect of non-condensable gas on cavitation in positive displacement pumps. Open Eng 2015; 5: 323-331.

14. Tsukiji T, Nakayama K, Saito K, Yakabe S. Study on the cavitating flow in an oil hydraulic pump. In: 11th International Conference on Fluid Power and Mechatronics, Beijing, China, 2011.

15. Roemer DB, Pedersen HC, Andersen TO. Simulation of dynamic behaviour of a digital displacement motor using transient 3D Computational Fluid Dynamics analysis, In: ASME/BATH 2013 Symposium on Fluid Power & Motion Control, Florida, USA, 2013.

16. Husmeier F, Sampl P, Platz HL, Greif D. Numerical simulation of compressible multi-phase flow in high-pressure fuel pump, In: 4th Joint US-European Fluids Engineering Division Summer Meeting, Chicago, USA, 2014.

17. Brennen C. Cavitation and Bubble Dynamics. London: Oxford University Press, 1995.

18. Dular M, Stoffel B, Sirok B. Development of a cavitation erosion model, Wear 2006; 261: 642-655.

19. Fortes-Patella R., Challier G., Reboud Jl., Archer A., Cavitation erosion mechanism: Numerical simulations of the interaction between pressure waves and solid boundaries, In: 4th International Symposium on Cavitation, Pasadena, USA, 2001.

20. Li Z. Assessment of cavitation erosion with a multiphase RANS, PhD Thesis, Delft Univ., Netherlands, 2012.

21. Koukouvinis P, Bergeles G, Gavaises M. A cavitation aggressiveness index with the Reynolds averaged Navier Stokes methodology for cavitating flows. J Hydrodyn 2015; 24: 579-586.

22. Timushev SF, Knyazev VA, Panaiotti SS, Soldatov VA., Rohatgi US. Numerical procedure for assessment of centrifugal pump cavitation erosion, In: ASME International Mechanical Engineering Congress and Exposition, Boston, USA, 2008.

23. Sedlář M, Zima P, Bajorek M, Krátký T. CFD analysis of unsteady cavitation phenomena in multistage pump with inducer. IOP Conf Ser: Earth Environ Sci 2012; 15: 062024.

24. ANSYS Inc. ANSYS Fluent 16, 2013.

25. Coutier-Delgosha O, Reboud JL, Delannoy Y. Numerical simulation of the unsteady behaviour of cavitating flows. Int J Num Methods Fluids 2003; 42: 527-548.

26. Dular M, Delgosha OC. Numerical modelling of cavitation erosion. Int J Num Methods Fluids 2009; 61: 1388–1410.

27. Menter FR, Egorov Y. The Scale-Adaptive Simulation Method for Unsteady Turbulent Flow Predictions. Part 1: Theory and Model Description. J Flow Turbulence Combust 2010; 85: 113-138.

28. ANSYS Inc. ANSYS Fluent 16 Theory Guide, 2013.

29. Dular M, Coutier-Delgosha O. Numerical modelling of cavitation erosion. Int. J. Num. Meth. Fluids 2009; 61:1388–1410.

30. Egerer CP, Hickel S, Schmidt SJ, Adams NA. Large-eddy simulation of turbulent cavitating flow in a micro channel. Phys. Fluids 2014; 26: 085102.

31. Washio S. Recent Developments in Cavitation Mechanisms: A Guide for Scientists and Engineers,1st Ed., Elsevier 2014: 133-157.

32. Kolev NI, Multiphase Flow Dynamics 3: Turbulence, Gas Absorption and Release, Diesel Fuel Properties. Heidelberg: Springer, 2007.

33. Koukouvinis P, Naseri H, Gavaises M. Performance of turbulence and cavitation models in prediction of incipient and developed cavitation. Int J of Engine Res 2016; 1-18.

34. Giannadakis E, Gavaises M, Arcoumanis C. Modelling of cavitation in diesel injector nozzles, J Fluid Mech 2008; 616: 153–193.

35. Koukouvinis P. and Gavaises M. Simulation of throttle flow with two phase and single phase homogenous equilibrium model. J Phys Conf Ser 2015; 656: 012086.

36. Mencinger J. An Alternative Finite Volume Discretization of Body Force Field on Collocated Grid, in R. Petrova (Ed.) "Finite Volume Method - Powerful Means of Engineering Design". 1st Ed., InTech, 2012.

37. Ivings MJ, Causon DM, and Toro EF. On Riemann solvers for compressible liquids. Int J Num Methods Fluids 1998; 28: 395-418.

38. Toro, EF. Riemann Solvers and Numerical Methods for Fluid Dynamics: A Practical Introduction, Heidelberg: Springer, 2009.

39. Batchelor GK. An Introduction to Fluid Dynamics. London: Cambridge University Press, 2000.

40. Jeong J and Hussain, F. On the identification of a vortex. J Fluid Mech 1995; 285: 69–94.